

Osiris-REx Balloon Recordings: Scattering Wavefield

Jonathan M Lees¹, Keehoon Kim⁴, Daniel C. Bowman², Elizabeth A. Silber³, and
Siddharth Krishnamoorthy⁵

¹University of North Carolina, Chapel Hill

²Pacific Northwest National Laboratory

³Sandia National Laboratories

⁴Lawrence Livermore National Laboratory

⁵NASA Jet Propulsion Laboratory

December 12, 2025

1 Introduction

The re-entry of the OSIRIS-REx satellite on September 24, 2023, represented an unprecedented opportunity for seismologists and acoustic scientists to study wave propagation from 60 km altitudes down to the surface of the Earth over eastern Nevada [Silber and Bowman, 2025]. Numerous teams launched extensive deployments including a variety of seismic and acoustic instrumentation in anticipation of shock waves and sonic booms created by the incoming rocket, traveling at speeds of 10 km/s, creating a shock wave recorded on microphones and seismometers alike.

17 Descriptions of the various ground deployments is well documented in several publications (see,
18 [Silber et al., 2024; Silber and Bowman, 2025; KC et al., 2025]) so we will not repeat here. Floating
19 acoustic stations, in the form of elevated balloon deployments, recorded shock waves directly from
20 the 60 km elevated source as well as reflections from the ground desert floor. Comparison of
21 reflected versus direct arrivals is the subject of a previous paper [Bowman et al., 2025] where
22 frequency dependence of amplitude decay is documented at two balloon stations at 1.7 km and 24
23 km elevation respectively.

24 This paper focuses on the wave propagation and scattering resulting from topographic varia-
25 tions in Nevada (Figure 1), and shows that rough terrain can have a critical influence on reflected
26 and scattered waves. Topography and infrasound has been studied by numerous investigators in-
27 cluding [Bishop et al., 2022; Khodr et al., 2022] Balloon recordings of topographic scattering of
28 chemical explosion sources in Sweden [Bird et al., 2022] suggest that ground scattering can have
29 critical impact on waves recorded in the stratosphere [Blom, 2020]. In the following we show that
30 shockwaves produced by the re-entry of the OSIRIS-REx capsule reflects at ground surface with
31 high impedance when the ground is relatively flat though scatters significantly when the terrain is
32 rough and mountainous.

33 This paper focuses on the wave propagation and scattering results from topographic variations
34 in Nevada (Figure 1), and shows that rough terrain can have a critical influence on reflected and
35 scattered waves. Topographic effects for infrasound propagating near the surface have been studied
36 by numerous investigators. It is well known that infrasound amplitudes and periods near sources
37 or receivers can be drastically altered by topographic diffraction and obstruction [Kim and Lees,
38 2014; Kim et al., 2015; Kim and Lees, 2015; Kim and Rodgers, 2016; Khodr et al., 2022]. Numerical
39 modelings also suggested that infrasound propagating in low-altitude troposphere can be scattered
40 by surface topography [de Groot-Hedlin, 2017; Bishop et al., 2022].

41 Unlike infrasound near the surface or in low-altitude troposphere, long-range infrasound prop-

agation is primarily governed by the atmospheric stratification [Evers and Haak, 2009; de Groot-Hedlin et al., 2009]. Due to the efficient waveguide by the temperature and wind gradients in the atmosphere, infrasound in the stratosphere can travel for hundreds of kilometers without significant loss of energy. In the long-range propagation, the stratospheric infrasound often experiences multiple reflections between the upper waveguide and the Earth’s surface. While those high-altitude propagation may not be directly affected by the surface conditions, recent studies with numerical modeling showed that reflection off the surface and resultant amplitudes can be notably different depending on surface topography [Blom, 2020; Bishop et al., 2024]. Our observation from the field experiment is the direct evidence of topographic impact on infrasound reflection off the surface. The stratospheric phase of infrasound is often critical to remote detection and identification of events [Blom et al., 2018; Kim, 2025], and quantitative characteristics of the surface reflection can affect the monitoring capability of global infrasound network [Christie and Campus, 2009; Le Pichon et al., 2012; Silber, 2024].

1.1 Review of balloon deployments

Deployments of high altitude balloons in the past ten years have become common. Several field campaigns indicate that infrasound monitoring in the lower stratosphere records acoustic wavefields with fidelity corroborated by ground truth [Bowman and Lees, 2015, 2017; Bird et al., 2022; Popenhagen et al., 2023]. Atmospheric recordings with floating stations provide an additional dimension to the standard ground based field campaigns. Balloons in motion, however, require special handling as meteorological conditions change and control of the unmanned floating stations, in this study was not available. In general, balloons at float status can avoid wind noise, although during ascent and descent relative motion can introduce noise as well as transient gusts.

64 1.2 Instrumentation

65 A variety of sensors and digitizers were deployed for the airborne part of the OSIRIS experiment.
66 Payloads were prepared in advance and attached to different balloons targeting various altitudes.
67 A table summary of deployment parameters is included as Table 1. As the focus of this paper is
68 BREX1-3 we outline here the main differences: BREX3 was recorded with InfraBSU microphones
69 [Marcillo et al., 2012] on DiGOS (DATA-CUBE) digitizers sampling at 400Hz. The 3-channel
70 digitizers recorded infrasound on two co-located channels, with the polarity reversed on one. The
71 reversed polarity channel was flipped and added to the first channel, for noise reduction. Stations
72 BREX1 and BREX2 were recorded with GEM systems [Anderson et al., 2018] which include a
73 microphone and digitizer, recording at 100 samples/s. GPS antennas record station locations and
74 timing as balloons rise and reach float elevation.

75 The stations were tethered to solar balloons launched at sunrise and designed to reach altitudes
76 between 20-30 km elevation. Table 1 includes the times and locations of each balloon station
77 at the time of the arrival of the direct wave from OSIRIS-REx. Elevations range from 21-27 km
78 above the ground, such that the horizontal distance to the source varies from 9-29 km with elevation
79 changes 24-30 km (Table 2). BREX1 is 17.8 and 8.5 km from BREX2 and BREX3, respectively.
80 Locations and 3D perspective plots of the deployment at the time of recording is presented in Figure
81 2.

82 2 Topographic Effects on Reflected Waves

83 The three floating stations in the northeast region of the deployment (BREX1-3) form an interesting
84 cluster. All three stations recorded sharp, unmistakable first arrivals from the direct OSIRIS shock
85 wave (Figure 3). Observed amplitude differ only slightly for the direct wave arrivals. Very clear,

86 high signal/noise ratio, reflections signals are pronounced on stations BREX2 and BREX3. On
87 BREX1, however, the reflected signal is significantly diminished (We emphasize that BREX1 and
88 BREX2 have the same GEM recording systems, where as BREX3 includes an InfraBSU sensor. See
89 discussion in the Instrumentation section.) BREX3 appears to be more sensitive to wind gusts and
90 clearly shows transient pressure variation bursts designated as noise.

91 To investigate the source of this discrepancy we employ a finite difference time-domain wave
92 propagation code, ElAc [Kim and Lees, 2014; Kim and Rodgers, 2016; Petersson and Sjögreen,
93 2018] . ElAc solves the seismic wave equations for solid media and the linearized Euler equation
94 for acoustic pressures in air. ElAc discretizes a spatial domain in a curvilinear grid which follows
95 terrain relief and can minimize numerical scattering due to stair-case approximation of surface
96 topography. A slightly smoothed topographic terrain was used as the surface and a line source
97 coded into the 3D wave propagation code was used. A line source is implemented by distributed
98 point sources following the trajectory of the incoming rocket. Each point source is represented by
99 a gaussian function and injected into the domain at the speeds between 6.5 – 6.9 km/s with Mach
100 numbers between 21 – 22. The shock wave angle of attack is in the range of 2.7° , suggesting that a
101 cylindrical source model is appropriate for simulation. Two line source models (5s and 1Hz corner
102 frequencies) were examined , although here we present the 1Hz version, as it is consistent with the
103 1Hz high-pass filter used in the presentations above.

104 The ElAc simulation code used a grid spacing of 25m for spatial discretization, in a $65km \times$
105 $45km \times 70km$ dimension (East, North, Elevation) modeling domain. For the simulation we used a
106 USGS NED elevation model and GFS NOAA meteorological model [Rutledge et al., 2006] for the
107 day and location of the event. Output traces were collected at 1 km spacing (Figure 4) at 22 km
108 elevation illustrating a simulated cross section perpendicular to the cylindrical source. The 22 km
109 level for the output traces is a compromise of the three station elevations (22.6, 26.9 and 21.2 km)
110 when the shock wave passed, and is closer to BREX1. Stations BREX2 and BREX3 has a clear
111 arrival at the times predicted for a wave reflected at the Earth’s surface . (Station BREX2 exhibits

several other noise pulses, attributed to wind disturbance.) All three stations show an extended coda following the reflection.

A significant difference in reflected arrivals is clear from visual inspection of the observed time series (Figure 3). Measures comparing the observed RMS (Root-Mean-Square) and Peak-Peak ratios of signal versus noise shows a marked difference at BREX1 versus BREX2 and BREX3 (Table 3). The lack of a clear reflection on BREX1, following the direct arrival, suggests that pronounced waveform distortion has occurred at this balloon location that is not evident elsewhere, especially in the nearby floating stations. We observed an extended scattered wave train at the time where the predicted arrival should arrive, indicating the arrival of diffuse signals, considerably diminished following the initial N-wave impacting the surface. At the time of the shock wave propagation, BREX1 was located above a range of exposed mountains, typical of Nevada’s basin and range tectonics. While there may be contrasts of variable impedance in the basin and range region, we suspect those variations are of lesser import than topographic and scattering effects due to significant elevation, rough terrain, and steep slopes below BREX1. Stations BREX2 and BREX3, on the other hand, appear to be floating above much flatter topography where basin geometry dominated (see contours in Figure 2).

3 Observations

Time series of the three stations is presented in Figure 3 where direct and reflected arrivals are indicated by arrows. Predicted reflection arrival times are estimated using simple atmospheric models with rocket and balloon locations at the re-entry times.

To test for the influence of topographic relief on reflects at BREX1 we simulated wave propagation with a standard DEM using 9/24/23 meteorological models for the atmosphere at BREX1

location. A cross section of the simulation is shown in Figures 5 and 6, showing the diminished amplitudes above the topographic high at 246 s following the shock wave initiation. The amplitudes are diminished due to scattering along the range which has 2-3 km elevation variation compared to nearby basins. Each of the panels show significant scattering: waves are critically diminished for waves reflecting directly below the rocket trajectory where elevations are high and topography is rough.

Synthetic time-series were produced for the three stations near this vicinity (Figure 5). Stations BREX3 and BREX4 [BREX2 and BREX3?](#) show strong reflections, comparable to the observed reflections recorded in the balloon observation. BREX1 is considerably attenuated by contrast. While the synthetic is clearly reduced in amplitude on BREX1, it does not exhibit as much attenuation as the observed signals. The coda of acoustic energy following the main reflected arrival is evident on all three synthetics and observed on the balloon stations, suggesting that nearby range reflected off the topography is present. (BREX3 sensors differed from BREX1 and BREX2: other, unrelated, noises are present between direct and reflected wave arrivals.)

We can compare the amplitudes and the standard deviations of the observed reflected arrival following the respective direct arrivals and compare with the synthetic amplitudes derived via wave propagation. All three stations have clear direct arrivals from the OSIRIS-REx shock wave (Figures 6 and 7).

Stations BREX3 and BREX4 have strong, impulsive wave-forms following reflection off the desert floor, each arriving at the appropriate time, based on acoustic wave propagation. For BREX3 and BREX2 the ratio of root-mean-square reflected to direct arrival for observed amplitude is 0.47 and 0.61 , respectively. Compare these with the relatively low RMS ratio of BREX1, 0.386 . A similar observation is found comparing the the peak-peak amplitude at three floating stations, namely for BREX2(0.58) and BREX3 (0.47) , versus BREX1 (0.117). Wave propagation modeling produces as similar pattern, i.e. with a reduced (although not as prominent) arrival at the reflection of BREX1

159 as compared to BREX2 and BREX3. For easy comparison, see Table 3.

160 4 Discussion

161 Other studies suggest that topographic effects on infrasound waves have a considerable influence. In
162 a multi-balloon field deployment in Sweden sensors were deployed 100 m apart along tethers hanging
163 from the gondola. Comparing arrivals at the balloons, delayed due to sensor separation, researchers
164 found [Bird et al., 2022] that scattering associated with rough terrain had a critical impact on coda
165 wave arrivals. In those studies, however, signals were generate by chemical explosion on the surface,
166 making it difficult to associate a specific source of the scattering. In the presentation here the shock
167 wave source at 50+ km elevation is orders of magnitude louder, arriving (nearly) directly above
168 the floating stations. This unique situation allows us to make precise comparisons of direct and
169 scattered waves.

170 From visual inspection and direct numerical comparison we observe a marked reduction in
171 amplitude and power in the the reflected waves at BREX1 versus BREX3 and BREX2. The
172 primary difference between these 3 floating stations is that station BREX1 has drifted to a location
173 above a mountain range as compared to the desert flats where the other two stations remained.
174 Synthetic wave propagation confirms this observation: the synthetic waveform at station BREX1 is
175 significantly reduced compared to the others. Waveform animation is included as digital supplement
176 showing the clear reduction of amplitudes above the mountainous regions. These confirm the
177 assumption that surface scattering played a significant roll in attenuating reflection and subsequent
178 wave propagation.

179 Topographic effects on infrasound propagation have been widely discussed, based mainly on
180 ground based observations and modeling [Chimonas, 1977; McKenna et al., 2012; Lacanna et al.,

2014]. These deployments showed that considerable distortion of acoustic infrasound waves occur when significant topographic variations (mountains, ridges) interact with the propagating waves. Distortions can affect estimation of source parameters with profound effect on monitoring capabilities. In volcanic regions waveform simulation is strongly dependent on topographic effects [Kim and Lees, 2014; Kim et al., 2015; Kim and Lees, 2015; Kim and Rodgers, 2016]. Yield estimates and source time function extraction for volcanic eruptions and nuclear and chemical explosions can be severely compromised by topographic effects [Vergoz et al., 2022; Kim and Lees, 2014, 2015; Toney et al., 2023].

In this paper, however, a unique source (OSIRIS-REx) provides an impulsive broadband source propagating directly into a floating array above the Nevada desert floor. The clear reflected waves (or lack thereof) illustrate, with great clarity, the severe effect the topographic variation has on the scattered waves once they interact with the surface. Ground based arrays like those cited above locate the stations on topographically challenging locations, especially in volcano regions. The floating array discussed here has the advantage of isolation from the terrain variations that cause local perturbations of the wavefield. (of course, floating balloons have their own peculiar set of noise effects). Furthermore, the OSIRIS-REx re-entry shockwave source is also far from any distortion due to topography.

Synthetic wave propagation of the OSIRIS-REx re-entry provides a means to monitor the pressure in the computational domain at ≈ 1 second time steps. An example of the wavefield variations at the desert surface and along two cross sections focussed on the point where rocket trajectory is perpendicular to the projection of the BREX1 balloon are presented in Figure 8. The three snapshots are selected from an animation of the wavefield which is presented as supplemental material. The first snapshot shows the direct wave propagating away from the rocket trajectory as a cylindrical wave. The amplitude of the wave is arbitrary since we do not have strong constraints on the amplitude of the source and source-time-function. The second snapshot ($T=165s$) shows the pressure wave field just as it impinges on the desert surface. There is a marked contrast where

207 the desert floor is flat, sand compacted terrain versus the rough topography of the mountainous
208 region directly below OSIRIS-REx at that time. The clear, considerable scattering and wavefield
209 distortion is evident in the surface image as well as the cross sections as the wave reflects off the
210 surface. The propagation of this distorted field can be seen in the third snapshot where a noticeable
211 'hole' is propagated skyward. Locations of the three observation balloons is marked on the map
212 view and the projected onto the cross sections.

213 Synthetic wavefield models show that when a direct wave strikes significant topography reflected
214 signals are dissipated, resulting in diffuse and complex wave patterns. Simulated wave propagation
215 presented here does not account for the complete attenuation of the wavefield at BREX1, compared
216 to BREX2 and BREX3. Rather, the reflected signal is diminished, though not as much as recorded in
217 the observed signals. We suspect that topographic scattering only accounts for part of the wavefield
218 loss. We suspect the loss of signal is due to other effects (turbulence, atmospheric absorption, etc.)
219 not accounted for in the wave propagation finite difference models.

220 This example illustrates how topographic effects are critical for waveform analysis of low fre-
221 quency acoustics over 100km scale regions. We provide here a case study that highlights these effects
222 and suggests that further study is warranted as observation and simulations show discrepancy that
223 we have not explained.

224 5 Conclusion

225 Investigation of the passage of shock waves from the OSIRIS-REx satellite on floating infrasound
226 stations ranging from 3.5 to 26 km elevations shows clear directed and surface reflected waves.
227 Acoustic power loss estimated at 13 to 70% is attributed to cylindrical spreading and loss due to
228 atmospheric friction as well as impedance loss to seismic and other absorption in the surface. Falloff

229 of log-spectral ratio between 10-15Hz of direct and reflected waves for BREX4 (3.5 km elevation
230 float) balloon was ~ -2 and for BREX3 (27 km float) frequency drop-off was -2.75 .

231 One station located above a mountainous range exhibited severe attenuation and scattering.
232 Compared to other stations above nearby basins we suggest that topographic scattering is the main
233 source of the loss of N-wave signal in the reflected waves. Simulations using finite-difference wave
234 propagation confirm the effects of topography and balloon location on reflected wave-forms.

235 6 Bibliography

236 References

- 237 Anderson, J. F., Johnson, J. B., Bowman, D. C., and Ronan, T. J. (2018). The gem infrasound logger and custom-built instrumentation.
238 *Seismol. Res. Lett.*, 89:153–164.
- 239 Bird, E. J., Lees, J. M., Kero, J., and Bowman, D. C. (2022). Topographically scattered infrasound waves observed on microbarometer
240 arrays in the lower stratosphere. *Earth and Space Science*, 9(4):e2022EA002226. e2022EA002226 2022EA002226.
- 241 Bishop, J. W., Blom, P., and Fee, D. (2024). Finite-frequency modeling of regional tropospheric infrasound using realistic atmospheres
242 and terrain. *The Journal of the Acoustical Society of America*, 155(1):128–144.
- 243 Bishop, J. W., Fee, D., Modrak, R., Tape, C., and Kim, K. (2022). Spectral element modeling of acoustic to seismic coupling over
244 topography. *Journal of Geophysical Research - Solid Earth*.
- 245 Blom, P. (2020). The influence of irregular terrain on infrasonic propagation in the troposphere. *The Journal of the Acoustical Society*
246 *of America*, 148:1984–1997.
- 247 Blom, P. S., Dannemann, F. K., and Marcillo, O. E. (2018). Bayesian characterization of explosive sources using infrasonic signals.
248 *Geophysical Journal International*, 215(1):240–251.
- 249 Bowman, D. C. and Lees, J. M. (2015). Infrasound in the middle stratosphere measured with a free-flying acoustic array. *Geophysical*
250 *Research Letters*, 42(22):10,010–10,017. 2015GL066570.
- 251 Bowman, D. C. and Lees, J. M. (2017). A comparison of the ocean microbarom recorded on the ground and in the stratosphere. *J.*
252 *Geophys. Res. Atmospheres*, 122:9773–9782.
- 253 Bowman, D. C., Lees, J. M., Silber, E. A., Krishnamoorthy, S., Fleigle, M. J., and LaPierre, J. R. (2025). A measurement of the infrasonic
254 reflection coefficient of flat ground. *GRL, in revision*.
- 255 Chimonas, G. (1977). A possible source mechanism for mountain-associated infrasound. *Journal of the Atmospheric Sciences*, 34:806–811.
- 256 Christie, D. R. and Campus, P. (2009). The ims infrasound network: Design and establishment of infrasound stations. In *Infrasound*
257 *monitoring for atmospheric studies*, pages 29–75. Springer.
- 258 de Groot-Hedlin, C. D. (2017). Infrasound propagation in tropospheric ducts and acoustic shadow zones. *The Journal of the Acoustical*
259 *Society of America*, 142(4):1816–1827.
- 260 de Groot-Hedlin, C. D., Hedlin, M. A., and Drob, D. P. (2009). Atmospheric variability and infrasound monitoring. In *Infrasound*
261 *monitoring for atmospheric studies*, pages 475–507. Springer.
- 262 Evers, L. G. and Haak, H. W. (2009). The characteristics of infrasound, its propagation and some early history. In *Infrasound monitoring*
263 *for atmospheric studies*, pages 3–27. Springer.

264 KC, R. J., Wilson, T. C., Fox, D., Spillman, K. B., Garcés, M. A., and Elbing, B. R. (2025). Acoustic observations of the osiris-rex
 265 sample return capsule re-entry from wendover airport. *Seismological Research Letters*.

266 Khodr, C., Green, D. N., and Azarpeyvand, M. (2022). Three-dimensional topographic effects on infrasound propagation across Ascension
 267 Island. *Geophysical Journal International*, 231:1558–1572.

268 Kim, K. (2025). Full-waveform simulation of infrasound propagation in the atmosphere: A case study of the 2023 april 20 spacex starship
 269 explosion. *Advances in Astronomy*, 2025(1):5540281.

270 Kim, K., Fee, D., Yokoo, A., and Lees, J. M. (2015). Acoustic source inversion to estimate volume flux from volcanic explosions.
 271 *Geophysical Research Letters*, 42(13):5243–5249. 2015GL064466.

272 Kim, K. and Lees, J. M. (2014). Local volcano infrasound and source localization investigated by 3D simulation. *Seismological Research
 273 Letters*, 85(6):1177–1186.

274 Kim, K. and Lees, J. M. (2015). Imaging volcanic infrasound sources using time reversal mirror algorithm. *Geophysical Journal
 275 International*, 202(3):1663–1676.

276 Kim, K. and Rodgers, A. (2016). Waveform inversion of acoustic waves for explosion yield estimation. *Geophysical Research Letters*,
 277 43(13):6883–6890.

278 Lacanna, G., Ichihara, M., Iwakuni, M., Takeo, M., Iguchi, M., and Ripepe, M. (2014). Influence of atmospheric structure and topography
 279 on infrasonic wave propagation. *Journal of Geophysical Research: Solid Earth*, 119(4):2988–3005.

280 Le Pichon, A., Ceranna, L., and Vergoz, J. (2012). Incorporating numerical modeling into estimates of the detection capability of the
 281 ims infrasound network. *Journal of Geophysical Research: Atmospheres*, 117(D5).

282 Marcillo, O., Johnson, J. B., and Hart, D. (2012). Implementation, characterization, and evaluation of an inexpensive low-power low-noise
 283 infrasound sensor based on a micromachined differential pressure transducer and a mechanical filter. *J. Atmos. Oceanic Technol.*,
 284 29:1275–1284.

285 McKenna, M. H., Gibson, R. G., and Walker, B. E. (2012). Topographic effects on infrasound propagation. *The Journal of the Acoustical
 286 Society of America*, 131(1):35–47.

287 Petersson, N. A. and Sjögreen, B. (2018). High order accurate finite difference modeling of seismo-acoustic wave propagation in a moving
 288 atmosphere and a heterogeneous earth model coupled across a realistic topography. *Journal of Scientific Computing*, 74:290–323.

289 Popenhagen, S. K., Bowman, D. C., Zeiler, C., and Garcés, M. A. (2023). Acoustic waves from a distant explosion recorded on a
 290 continuously ascending balloon in the middle stratosphere. *Geophysical Research Letters*, 50(20).

291 Rutledge, G. K., Alpert, J., and Ebisuzaki, W. (2006). Nomads: A climate and weather model archive at the national oceanic and
 292 atmospheric administration. *Bulletin of the American Meteorological Society*, 87(3):327–342.

293 Silber, E. A. (2024). The utility of infrasound in global monitoring of extraterrestrial impacts: a case study of the 2008 july 23 tajikistan
 294 bolide. *The Astronomical Journal*, 168(1):17.

295 Silber, E. A. and Bowman, D. C. (2025). Along-trajectory acoustic signal variations observed during the hypersonic re-entry of the
296 osiris-rex sample return capsule. *Seismological Research Letters*.

297 Silber, E. A., Bowman, D. C., Carr, C. G., Eisenberg, D. P., Elbing, B. R., Fernando, B., Garcés, M. A., Haaser, R., Krishnamoorthy,
298 S., Langston, C. A., Nishikawa, Y., Webster, J., Anderson, J. F., Arrowsmith, S., Bazargan, S., Beardslee, L., Beck, B., Bishop,
299 J. W., Blom, P., Bracht, G., Chichester, D. L., Christe, A., Clarke, J., Cummins, K., Cutts, J., Danielson, L., Donahue, C., Eack, K.,
300 Fleigle, M., Fox, D., Goel, A., Green, D., Hasumi, Y., Hayward, C., Hicks, D., Hix, J., Horton, S., Hough, E., Huber, D. P., Hunt,
301 M. A., Inman, J., Islam, S. M. A., Izraelevitz, J., Jacob, J. D., Johnson, J., KC, R. J., Komjathy, A., Lam, E., LaPierre, J., Lewis,
302 K., Lewis, R. D., Liu, P., Martire, L., McCleary, M., McGhee, E. A., Mitra, I., Nag, A., Ocampo Giraldo, L., Pearson, K., Plaisir,
303 M., Popenhagen, S. K., Rassoul, H., Ronac Giannone, M., Samnani, M., Schmerr, N., Spillman, K., Srinivas, G., Takazawa, S. K.,
304 Tempert, A., Turley, R., Van Beek, C., Viens, L., Walsh, O. A., Weinstein, N., White, R., Williams, B., Wilson, T. C., Wyckoff, S.,
305 Yamamoto, M.-y., Yap, Z., Yoshiyama, T., and Zeiler, C. (2024). Geophysical observations of the 2023 september 24 osiris-rex sample
306 return capsule reentry. *The Planetary Science Journal*.

307 Toney, L., Fee, D., Schmandt, B., and Bishop, J. W. (2023). Examining infrasound propagation at high spatial resolution using a nodal
308 seismic array. *Journal of Geophysical Research: Solid Earth*, 128(11):e2023JB027314. e2023JB027314 2023JB027314.

309 Vergoz, J., Hupe, P., Listowski, C., Le Pichon, A., Garces, M., Marchetti, E., Labazuy, P., Ceranna, L., Pilger, C., Gaebler, P., Nasholm,
310 S., Brissaud, Q., Poli, P., Shapiro, N., De Negri, R., and Mialle, P. (2022). Ims observations of infrasound and acoustic-gravity waves
311 produced by the january 2022 volcanic eruption of hunga, tonga: A global analysis. *Earth and Planetary Science Letters*, 591:117639.

7 Tables

	Name	Minute	Second	Latitude	Longitude	Elev(km)	Sensor type	NA
1	BREX1	44.00	58.00	39.76	-114.86	22.64	Gem	Gem
2	BREX2	44.00	42.00	39.91	-114.78	21.16	Gem	Gem
4	BREX3	44.00	47.00	39.78	-114.78	26.86	InfraBSU	DATA-CUBE

Table 1: Station and Sensor Parameters of Floating Balloon Deployment

Source, km			Hoz Dist, km			Total Dist, km		
	Dist	Elev	BX1	BX2	BX3	BX1	BX2	BX3
BREX1	22.10	29.02	0.00	17.76	7.35	0.00	17.82	8.48
BREX2	8.86	29.56	17.76	0.00	14.56	17.82	0.00	15.64
BREX3	22.52	24.24	7.35	14.56	0.00	8.48	15.64	0.00

Table 2: Relative Distances Between Floating Stations and Line Source. First 2 columns are perpendicular distances from stations to the OSIRIS-REx line source. Columns labeled Hoz are mapview distances between stations in km. Total Distance includes the relative station elevation differences.

	obs RMS	obs P2P	syn RMS	syn P2P
BREX2	0.61	0.58	0.61	0.63
BREX3	0.47	0.47	0.49	0.69
BREX1	0.39	0.12	0.38	0.34

Table 3: Comparison of ratios of signal to noise for observed vs synthetic wave arrivals. RMS is the root-mean-standard deviation and P2P is the maximum peak-2-peak spread.

8 Figures

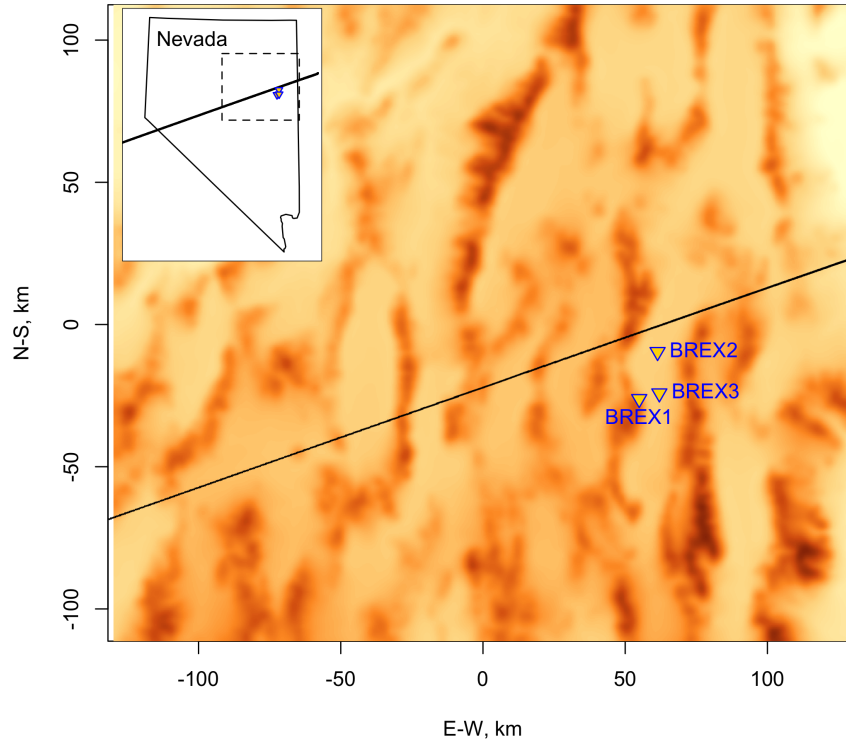


Figure 1: Plan view of balloon deployment during the reentry of OSIRIS-REx in September 2023. Locations correspond to the floating position of balloons when the satellite passed. The dark line represents the trajectory of the satellite. Inset shows region of Eastern Nevada. Stations BREX1-3 are the main focus of this paper, although signals were recorded on several other balloon stations. BREX1-3 were floating between 21-29 km altitude. Topographic relief is considerable in the basin and range region of Nevada. Blue arrows show direction of OSIRIS-REx trajectory.

Alt-text Topographic map of a region in Nevada, USA, with elevation or geological features represented by a color gradient-lighter tones indicating higher elevations. Axes are labeled 'E-W, km' and 'N-S, km' to show horizontal and vertical distances in kilometers. Three labeled points - BREX1, BREX2, and BREX3 - are marked in blue text across the map. A black diagonal line runs from the lower left to the upper right, possibly indicating OSIRIS-REx transect. In the upper left corner, an inset map of Nevada highlights the mapped area with a dashed box and a blue dot marking a specific location.

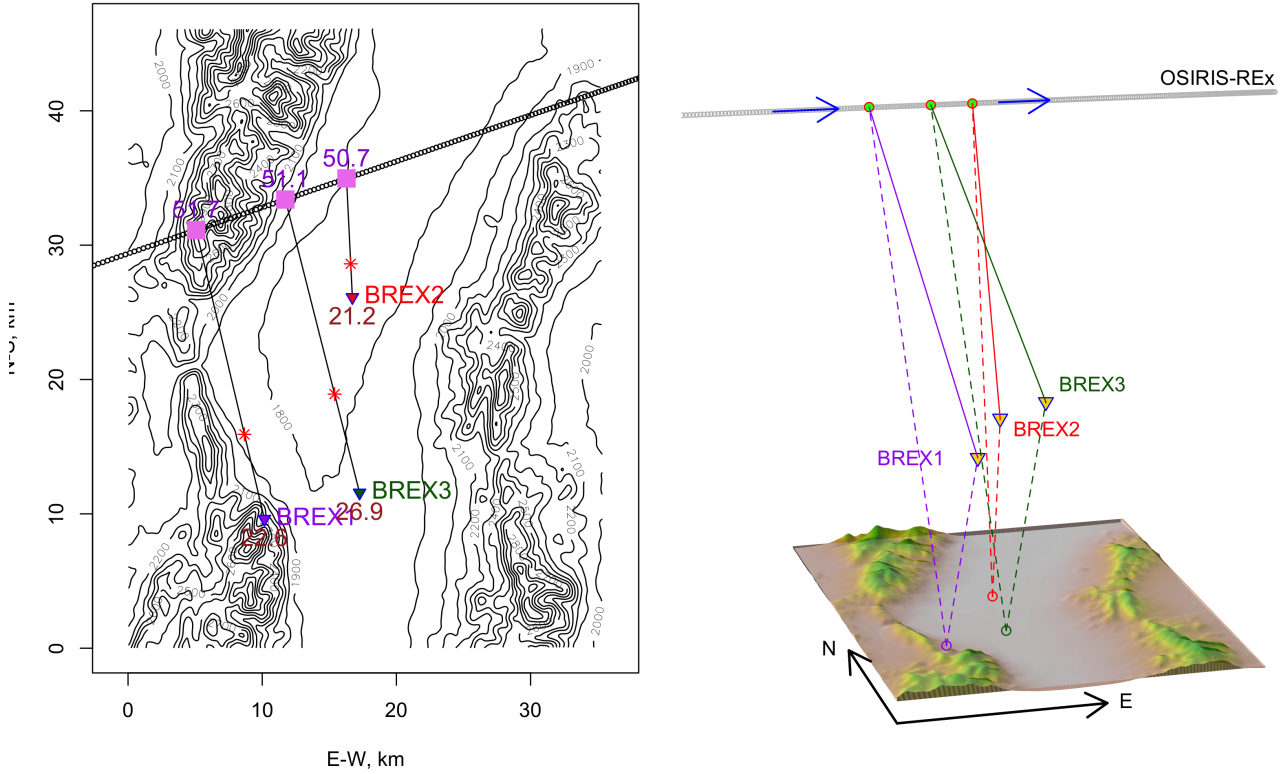


Figure 2: Zoom on geographic layout of the balloon field deployment relative to incoming OSIRIS-REx trajectory. Left: Topographic relief in the vicinity of BREX1-3. Contours range from 1.8km to 3.13km. Topographic relief presented here has been smoothed relative to the original ASTER data. Right: Perspective view, facing northeast, of balloon deployment during the passage of OSIRIS. Three stations are labeled in bold. Solid colored segments are direct arrival paths, dashed lines are simple bounce paths with the bounce point represented as a circle. BREX1 (22.64 km, purple) bounce point appears to align with a mountain range that has elevation variations up to 3000m. Stations BREX2 and BREX3 appear to bounce in desert valleys. Topographic relief is exaggerated by 3 for clarity.

Alt-text Detail of topographic contours with lines perpendicular showing red dots as bounce points. Elevations are posted as 22.6, 26.9 and 21.2 km.

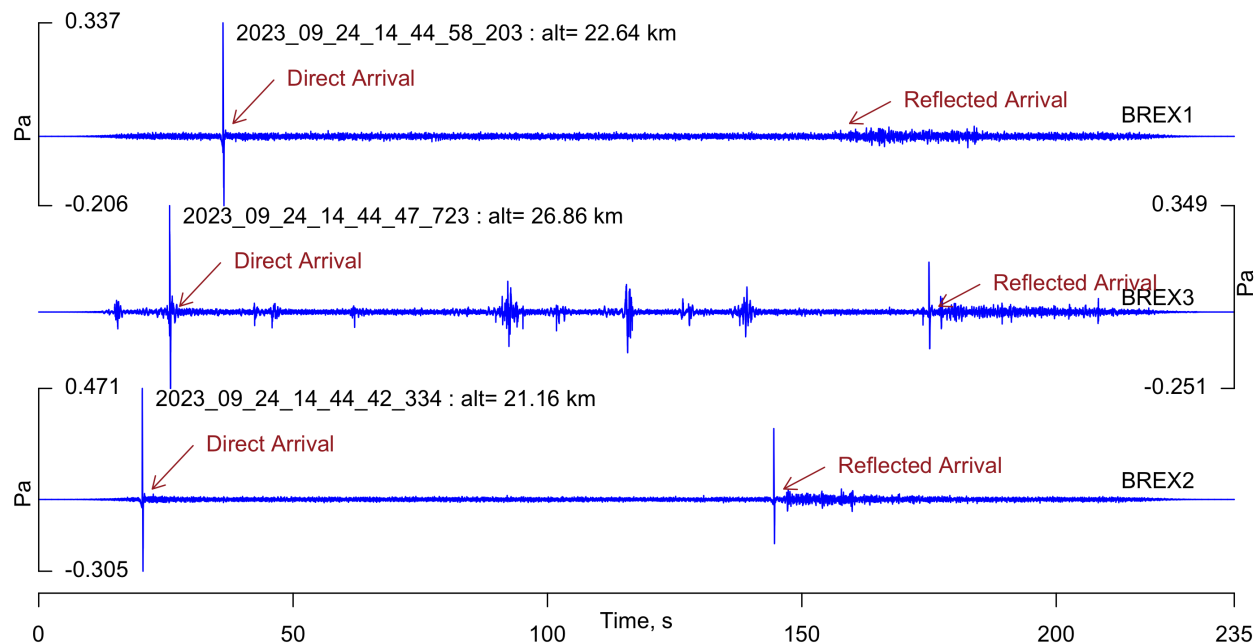


Figure 3: Three balloon recordings at the time of passage of OSIRIS, Sept. 24, 2023. Plotted in order of first arrival, from bottom to top. Direct arrivals and expected reflections are indicated by arrows. Balloons 1-3 are floating 21-26km. Note that BREX2-3 have clear sharp N-wave arrivals where expected, where as BREX1 has only a diffuse coda associated with scattering above severe topographic relief.

Alt-text Three acoustic time series (time versus Pascals) showing direct and reflected arrivals.

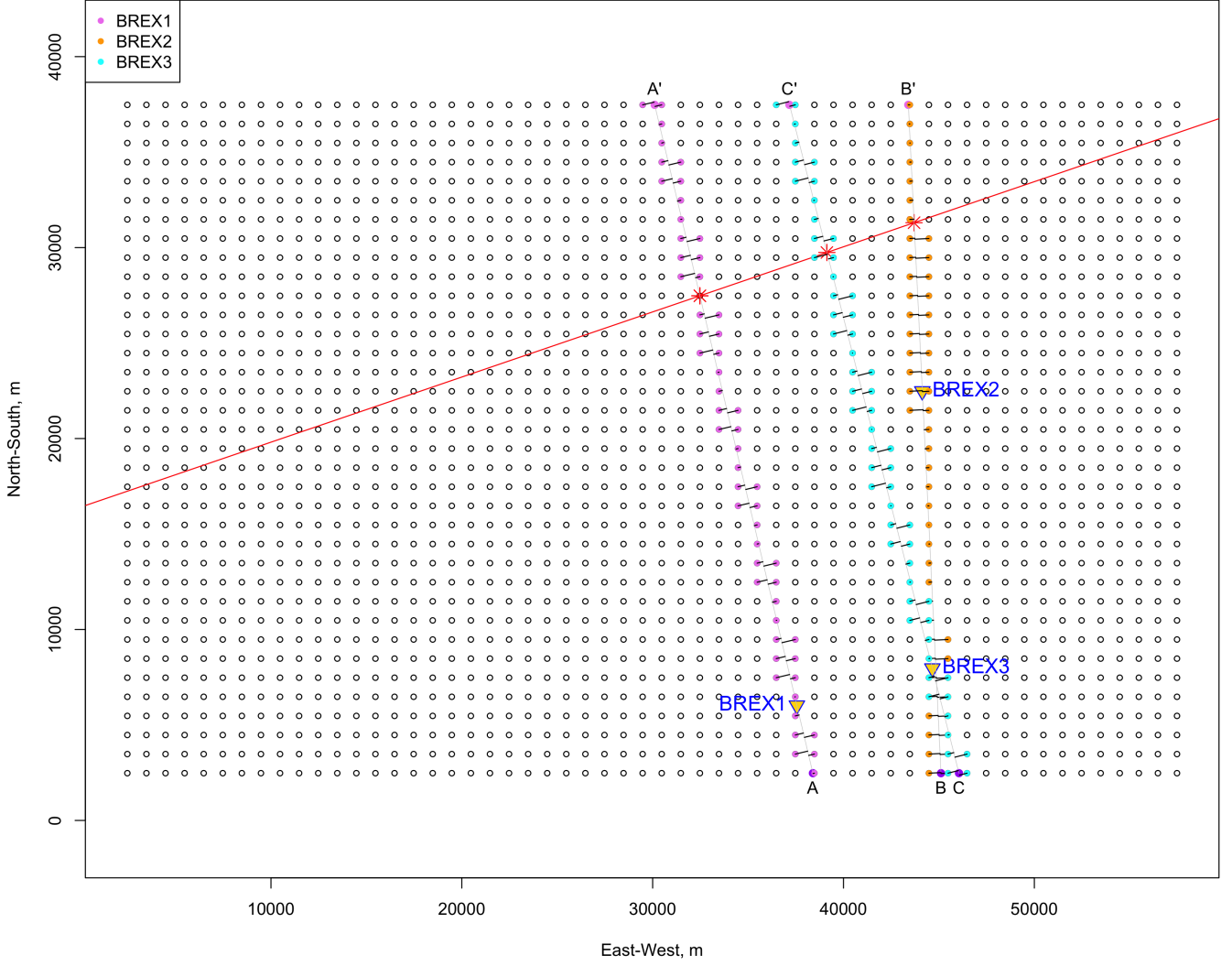


Figure 4: Grid plan (1×1 km spacing) at 22 km elevation where synthetic signals are displayed. Red line is the trajectory of the OSIRIS-REx re-entry trace. North-South Lines (A, B, C) represent perpendicular planes where cross sections are extracted. Acoustic signals within $0.75 \delta x$ from the grid are projected onto each line.

Alt-text Small dots in a rectangular grid show the model points where synthetic wave propagation were performed. A red east-west trending line shows the rocket trajectory. Colored dots show which traces were selected to plot in the cross section, projected onto corresponding perpendicular trace to rocket.

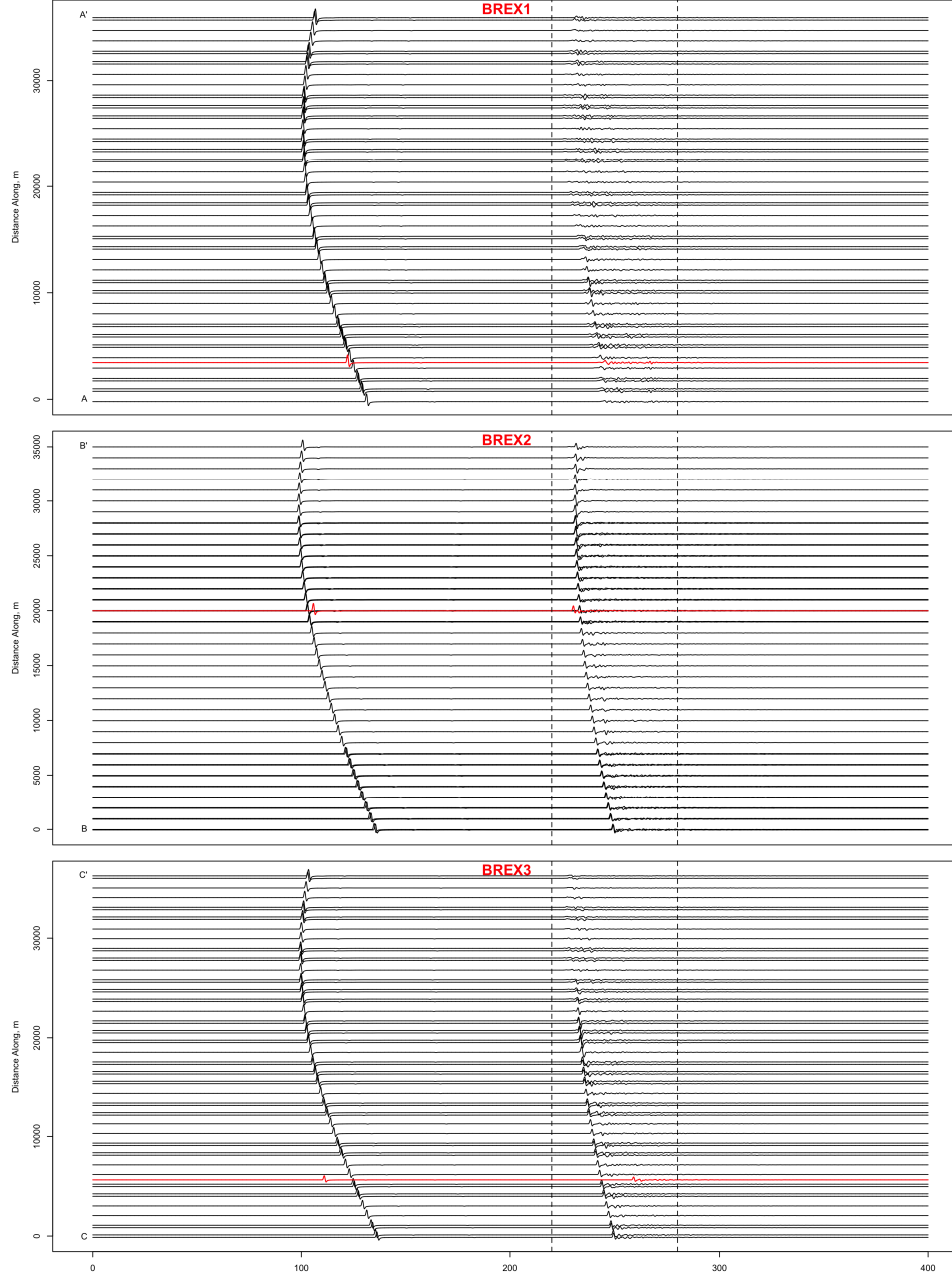


Figure 5: Synthetic Cross sections for three balloon stations. Top: A-A', BREX1. Center: B-B', BREX2. Bottom: C-C', BREX3. Cross section are extracted at 22km elevation, taken perpendicular to the cylindrical source of the OSIRIS-REx rocket. Vertical dashed lines show the section extracted for zoom in

Alt-text Three panels stacked vertically showing acoustic traces that show the prominent arcuate direct arrival and the return from the reflection on the surface. The lower two panels show strong reflection signals at BREX2 and BREX3. Traces on BREX1 are substantially diminished. Three red traces on each panel show the synthetic acoustic signals from each of the three balloon stations plotted alongside the synthetics.

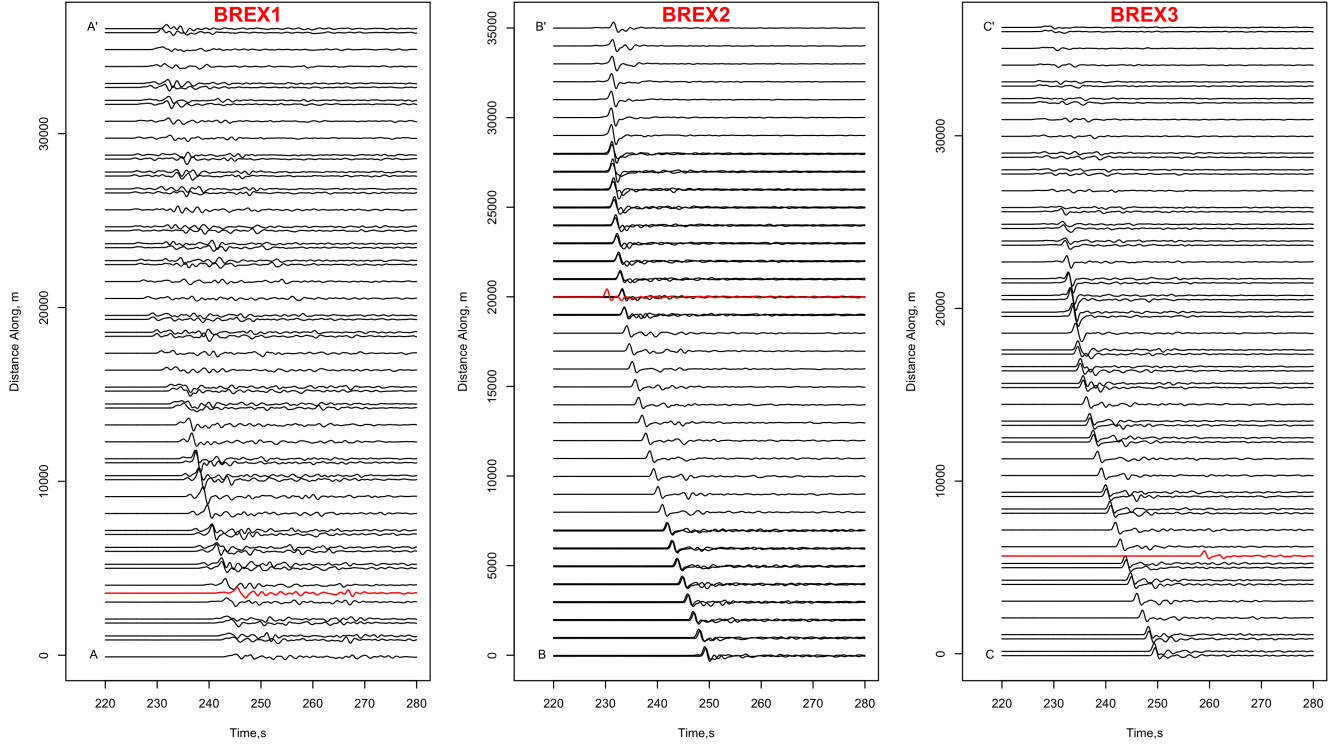


Figure 6: Zoom on Reflection of Synthetic Cross sections for three balloon stations. Top: A-A', BREX1. Center: B-B', BREX2. Bottom: C-C', BREX3. Cross section are extracted at 22km elevation, taken perpendicular to the cylindrical source of the OSIRIS-REx rocket.

Alt-text Three panels stacked vertically showing acoustic traces that show the prominent arcuate direct arrival and the return from the reflection on the surface. The lower two panels show strong reflection signals at BREX2 and BREX3. Traces on BREX1 are substantially diminished. Three red traces on each panel show the synthetic acoustic signals from each of the three balloon stations plotted alongside the synthetics.

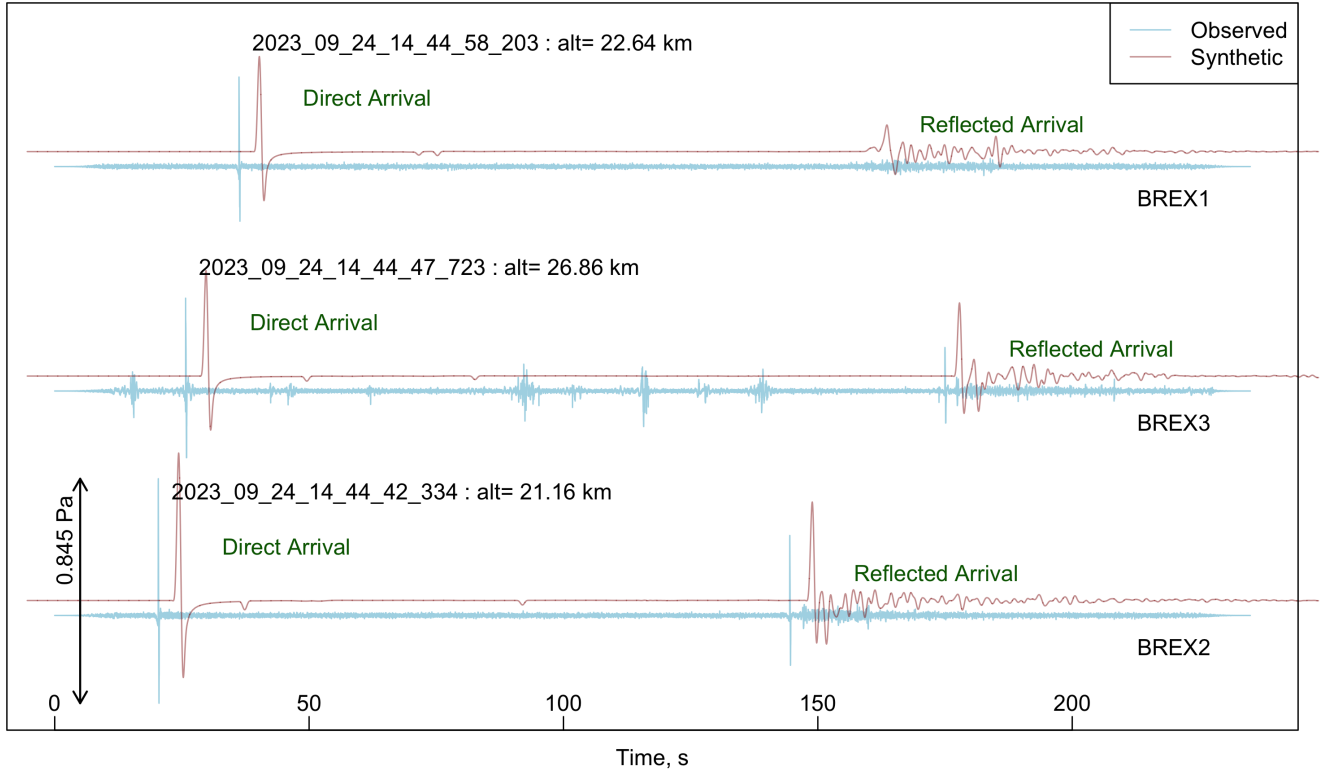


Figure 7: Comparison of observed versus synthetic wave-forms from OSIRIS-REx cylindrical wave propagation on September 24, 2023. Each synthetic has been shifted slightly in time and amplitude for ease of comparison. Amplitudes of the synthetic arrivals are arbitrary, so each is scaled to match the corresponding first arrival per station. The three panels are scaled per window so relative amplitudes are comparable. The diminished reflected arrival at station BREX1 is clearly notable in the observed signals, and significantly reduced in the synthetic. We surmise the reflected reduction is due to scattering along the mountainous terrain.

Alt-text Seismogram plot comparing observed (black) and synthetic (red) seismic wave-forms from three stations: BREX1, BREX3, and BREX2. Each subplot displays time in seconds on the x-axis and amplitude in Pascals on the y-axis, with a scale of 0.845 Pa. Event timestamps and altitudes are labeled: BREX1 (22.64 km), BREX3 (26.86 km), BREX2 (21.16 km). Green annotations mark "Direct Arrival" and "Reflected Arrival" phases, highlighting seismic wave propagation. The image visually contrasts real and modeled seismic data to assess model accuracy.

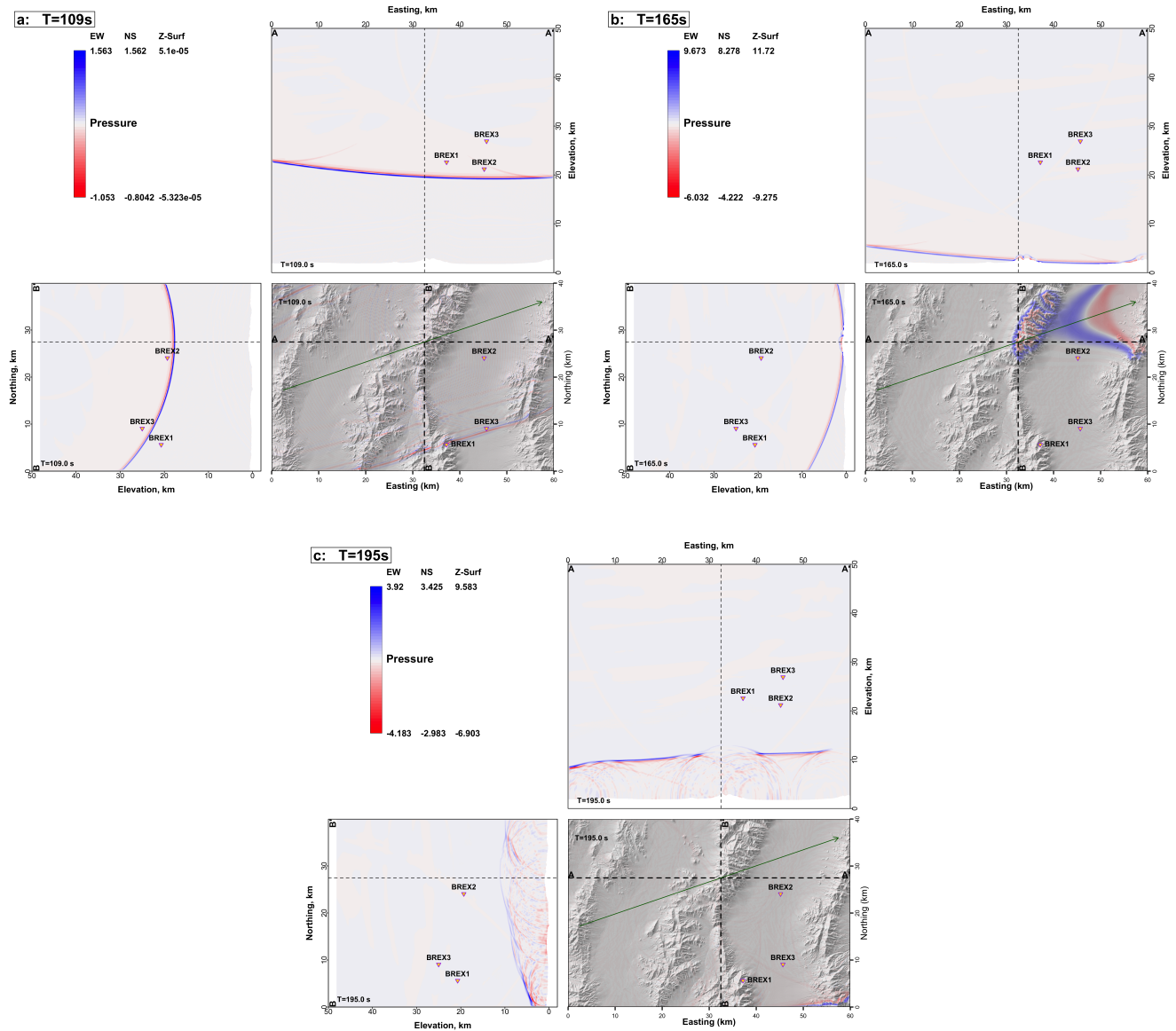


Figure 8: Three snapshots of the wave simulation. a: Direct wave passes b: Wave impinges on the desert surface. c: Reflected wave propagates skyward. Stations are horizontally projected onto the NS and EW cross sections. The green arrow indicates the trajectory of OSIRIS-REx. Cross sections are marked with dotted lines centered on the trajectory point designated as the source for BREX1.

Alt-text Three time snapshots showing topography and 2 cross sections. Each panels includes topography basemap color coded according to the pressure at the surface, and cross sections show direct and reflected acoustic waves. A fourth panel shows the color scale and quantitative ranges for the three images.